FULL PAPER

Advanced Asymmetric Supercapacitors Based on Ni(OH)$_2$/Graphene and Porous Graphene Electrodes with High Energy Density

Jun Yan, Zhuangjun Fan,* Wei Sun, Guoqing Ning, Tong Wei, Qiang Zhang, Rufan Zhang, Linjie Zhi,* and Fei Wei*

Hierarchical flowerlike nickel hydroxide decorated on graphene sheets has been prepared by a facile and cost-effective microwave-assisted method. In order to achieve high energy and power densities, a high-voltage asymmetric supercapacitor is successfully fabricated using Ni(OH)$_2$/graphene and porous graphene as the positive and negative electrodes, respectively. Because of their unique structure, both of these materials exhibit excellent electrochemical performances. The optimized asymmetric supercapacitor could be cycled reversibly in the high-voltage region of 0–1.6 V and displays intriguing performances with a maximum specific capacitance of 218.4 F g^{-1} and high energy density of 77.8 Wh kg^{-1}. Furthermore, the Ni(OH)$_2$/graphene//porous graphene supercapacitor device exhibits an excellent long cycle life along with 94.3% specific capacitance retained after 3000 cycles. These fascinating performances can be attributed to the high capacitance and the positive synergistic effects of the two electrodes. The impressive results presented here may pave the way for promising applications in high energy density storage systems.

Dr. J. Yan, Prof. Z. J. Fan, W. Sun, Prof. T. Wei
Key Laboratory of Superlight Materials and Surface Technology
Ministry of Education
College of Material Science and Chemical Engineering
Harbin Engineering University
Harbin 150001, P. R. China
E-mail: fanzhj666@163.com

Dr. G. Q. Ning
State Key Laboratory of Heavy Oil Processing
China University of Petroleum
Beijing 102249, P. R. China

Prof. L. J. Zhi
National Center for Nanoscience and Technology of China
Zhongguancun, Beiyitiao 11
Beijing 100190, P. R. China
E-mail: zhilj@nanoctr.cn

Dr. Q. Zhang, R. F. Zhang, Prof. F. Wei
Beijing Key Laboratory of Green Chemical Reaction
Engineering and Technology
Department of Chemical Engineering
Tsinghua University
Beijing 100084, P. R. China
E-mail: weifei@flotu.org

1. Introduction

Supercapacitors or electrochemical capacitors have attracted considerable attention in recent years because they can provide instantaneously a higher power density than batteries and higher energy density than conventional dielectric capacitors.[1–6] Therefore, they have been widely used in portable electronics, power back-up, electrical vehicles and various microdevices, where high power density and long cycle-life are desirable, and are considered to be the most important in next-generation energy storage devices.[7,8]

Although supercapacitors have a high power density, they usually suffer from a lower energy density than rechargeable batteries.[9] Advanced supercapacitors must be developed with higher operating voltage and higher energy without sacrificing the power delivery and cycle life to meet the energy demands for practical applications in the future.[10] The improvements of energy density (*E*) can be achieved by maximizing the specific capacitance (*C*) and/or the cell voltage (*V*) according to the following equation:[11,12]

$$E = 0.5CV^2 \qquad (1)$$

More recently, asymmetric supercapacitors have been found to be an effective alternative approach to increase the energy density of supercapacitors. These asymmetric supercapacitors consist of a battery-type Faradaic electrode (as the energy source) and a capacitor-type electrode (as the power source), simultaneously offering the advantages of both supercapacitors (rate, cycle life) and advanced batteries (energy density).[9] Therefore, asymmetric supercapacitors can make full use of the different potential windows of the two electrodes to provide a maximum operation voltage in the cell system, accordingly resulting in a greatly enhanced specific capacitance and significantly improved energy density.[13]

Hitherto, various materials such as transition metal oxides, metal hydroxides, and electronically conducting polymer materials have been investigated extensively for possible applications in asymmetric supercapacitors.[7,8] Among them, Ni(OH)$_2$ is one of the most promising candidates for its high theoretical

www.MaterialsViews.com

ADVANCED
FUNCTIONAL
MATERIALS
www.afm-journal.de

FULL PAPER

specific capacitance (2082 F g^{-1}).[1] Recently, an asymmetric supercapacitor with graphene/Ni(OH)$_2$ as the positive electrode and graphene/RuO$_2$ as the negative electrode[14] has been demonstrated to exhibit a high specific capacitance (ca. 153 F g^{-1}) and high energy (ca. 48 Wh kg^{-1}) at a voltage of 1.5 V in 1 M KOH aqueous solution. Inspired by the potential applications of Ni(OH)$_2$, numerous efforts have been recently devoted to the synthesis of Ni(OH)$_2$ nanostructures with different morphologies and structures, such as plateletlike,[15] flowerlike,[16,17] nanoparticles,[18] microspheres,[19] nanotubes,[20] and nanorods.[21] Among these different morphologies, flowerlike nanostructured Ni(OH)$_2$ has attracted considerable attention because of its short diffusion path lengths for both electrolyte ions and electrons, favoring the diffusion and migration of electrolyte ions during the rapid charge/discharge process and consequently improving the effective electrochemical utilization of Ni(OH)$_2$.[22]

Herein, for the first time, we report a novel strategy to prepare hierarchical flowerlike Ni(OH)$_2$ decorated on graphene sheets using a fast, facile, and cost-effective microwave heating method without the need for hard/soft templates or precipitate-controlling agents. The Ni(OH)$_2$/graphene hybrid material showed a high specific capacitance of 1735 F g^{-1} and high rate capability compared to a pure Ni(OH)$_2$ electrode. Moreover, an asymmetric supercapacitor based on Ni(OH)$_2$/graphene composite as the positive electrode and porous graphene as the negative electrode was successfully fabricated (**Figure 1**). Our optimized asymmetric supercapacitor showed a specific capacitance of 218.4 F g^{-1} and a maximum energy density of 77.8 Wh kg^{-1} based on the total mass of active materials at a voltage of 1.6 V.
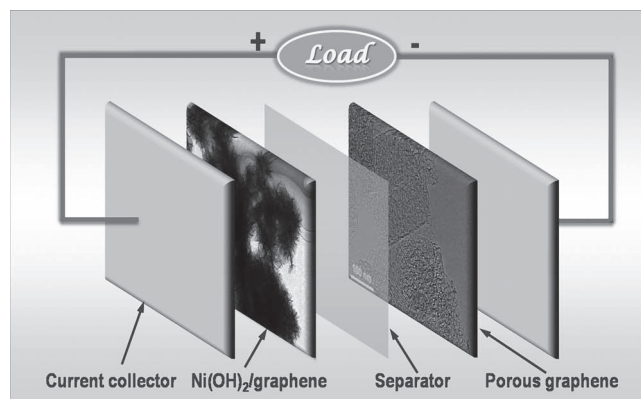
2. Results and Discussion

2.1. Positive Electrode Materials

Typical X-ray diffraction (XRD) patterns of the as-prepared hierarchical flowerlike Ni(OH)$_2$/graphene composite and free Ni(OH)$_2$ are shown in **Figure 2**a. It can be seen that the XRD pattern of the Ni(OH)$_2$/graphene composite is similar to that of free Ni(OH)$_2$, indicating that the Ni(OH)$_2$/graphene composite has been well synthesized. All of the reflections in the XRD pattern in Figure 2a can be indexed to rhombohedral α-Ni(OH)$_2$ with lattice parameters of $a = b = 3.08$ Å and $c = 23.41$ Å (JCPDS 38-715), which is in good agreement with the reported pattern for α-Ni(OH)$_2$.[23] The four characteristic peaks at 12.1°, 24.6°, 33.3°, and 59.4° correspond to the (003), (006), (101), and (110) diffraction planes, respectively. According to the Bragg formula, the calculated basal spacing is 0.73 nm, which is in accordance with the reported values.[23,24] It is noteworthy that the diffraction peaks of C for graphene could not be observed in the XRD
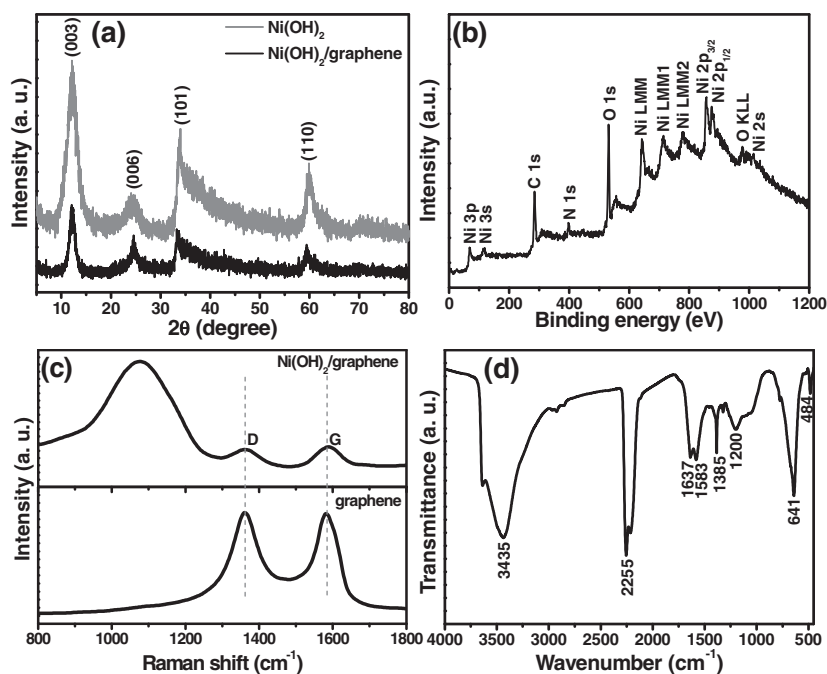

Figure 1. Schematic illustration of the as-fabricated asymmetric supercapacitor device based on Ni(OH)$_2$/graphene composite as the positive electrode and porous graphene as the negative electrode in 6 M aqueous KOH electrolyte.

pattern of the Ni(OH)$_2$/graphene composite, which is perhaps related to a more disordered stacking and quite uniform dispersion of the graphene sheets in the resulting composite. In addition, no peaks from other phases were detected indicating that the product is of high purity. Moreover, the relative intensity of the corresponding diffraction peaks for the Ni(OH)$_2$/graphene composite is significantly decreased compared to those of the pure Ni(OH)$_2$ sample, demonstrating a decrease in grain sizes of Ni(OH)$_2$ particles after decoration onto the graphene sheets. The average crystalline sizes of the synthesized samples

Figure 2. a) XRD patterns of pure Ni(OH)$_2$ and Ni(OH)$_2$/graphene composite. b) XPS spectrum of the prepared Ni(OH)$_2$/graphene composite. c) Raman spectra of the pristine graphene sheets and Ni(OH)$_2$/graphene composite. d) FTIR spectrum of the prepared Ni(OH)$_2$/graphene composite.

calculated from the (003) diffraction peak using Scherrer's formula are 14.2 and 11.5 nm for the pure $Ni(OH)_2$ sample and the $Ni(OH)_2$/graphene composite, respectively, which is consistent with the above XRD analysis.

In order to further understand the surface information of the obtained samples, X-ray photoelectron spectroscopy (XPS) was also carried out to analyze the composition of the particle surface (Figure 2b). It can be clearly seen that the survey spectrum of the $Ni(OH)_2$/graphene composite mainly shows carbon, oxygen, and nickel species as well as a small quantity of nitrogen, which comes from the precursor nickel nitrate hexahydrate. The peak located at 284.6 eV can be assigned to the characteristic peak of C 1s and a detailed analysis of the C 1s region indicates that there are still some residual oxygen-containing functionalities on the reduced graphene oxide sheets because of incomplete reduction (Figure 2b and Supporting Information Figure S1a). The Ni 2p XPS spectrum shows two major peaks with binding energies at 873.5 and 855.9 eV, corresponding to Ni $2p_{1/2}$ and Ni $2p_{3/2}$, respectively, with a spin-energy separation of 17.6 eV (Supporting Information Figure S1b), which is the characteristic of a $Ni(OH)_2$ phase and in good agreement with previously reported data.[23] This result is also consistent with the XRD analysis as mentioned above. It is worth noting that there are some extra lines marked as satellite peaks around the expected Ni $2p_{1/2}$ and Ni $2p_{3/2}$ signals in the Ni 2p region as shown in Figure S1b (Supporting Information).

The Raman spectra of pristine graphene and the $Ni(OH)_2$/graphene composite are shown in Figure 2c. It can be clearly seen that there are two broad peaks at 1361 and 1583 cm^{-1} in both samples, corresponding to the D and G bands of graphene, respectively. In the Raman spectrum, the G band represents the in-plane bond-stretching motion of the pairs of C sp^2 atoms (the E_{2g} phonons); whereas the D band corresponds to the breathing modes of rings or κ-point phonons of A_{1g} symmetry.[25] In addition, for the $Ni(OH)_2$/graphene composite, there is an additional broad peak centered around 1077 cm^{-1}, which may be attributed to the vibration of intercalated nitrate ions.[26]

To further confirm the XRD and Raman results, the composition of the as-prepared $Ni(OH)_2$/graphene composite was examined by Fourier transform infrared (FTIR) spectroscopy in the range of 400–4000 cm^{-1} and the results are shown in Figure 2d. The broad band at 3435 cm^{-1} corresponds to the O-H vibration of hydrogen-bonded hydroxyl groups and intercalated water molecules located in the interlamellar space of α-$Ni(OH)_2$.[16,23] The very strong absorption band at 2255 cm^{-1} is the typical vibration of C≡N triple bonds in the OCN^- anions, which are the byproducts of urea hydrolysis.[16] The weak bands around 1637 and 1583 cm^{-1} can be assigned to the bending mode of the interlayer water molecule and the
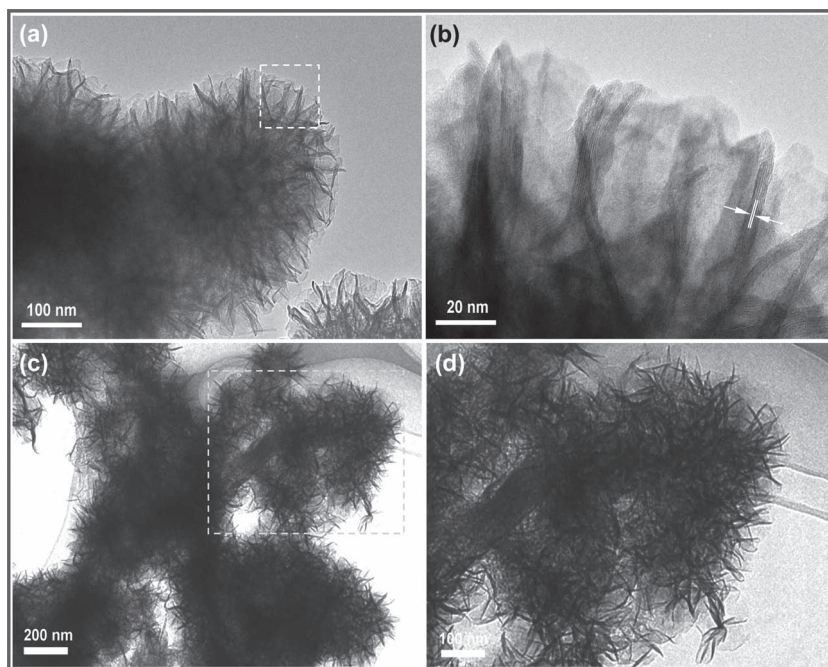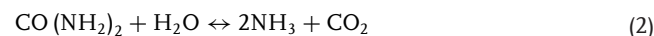

Figure 3. TEM images of a,b) $Ni(OH)_2$ and c,d) $Ni(OH)_2$/graphene composite. b) and d) are higher magnifications of the square frame regions in (a) and (c), respectively.

skeletal vibration of the carbon ring in the graphene sheets, respectively.[27] Additionally, the absorption band located at 1200 cm^{-1} is probably related to the presence of carbonate ions derived from the adsorption of atmospheric CO_2 or hydrolysis of urea.[16] Moreover, the band at 1385 cm^{-1} can be attributed to the interlayer nitrate anion,[16] whereas the two bands around 641 and 484 cm^{-1} are ascribed to the δ_{OH} and v_{Ni-OH} vibrations, respectively.[17,28]

The morphology and structure of the as-prepared samples were observed by transmission electron microscopy (TEM). **Figure 3**a clearly shows that the as-prepared $Ni(OH)_2$ sample is composed of many well-defined flowerlike architectures with diameters of 300 to 400 nm. It can also be observed that each flower is assembled by dozens of interconnected flake-like nanopetals with thicknesses of around 7 nm (Figure 3a, b). The distances between the lattice fringes is around 0.7 nm, corresponding to the d-spacing of the (003) plane of α-$Ni(OH)_2$, which is consistent with the XRD results. By incorporating graphene sheets, the flowerlike $Ni(OH)_2$ are well inherited and decorate homogeneously on the graphene sheets (Figure 3c). Interestingly, the diameters of these flowerlike structures decrease to 200–250 nm and the thickness of the nanoplatelets also decreases from 7 to 5 nm, indicating a homogeneous nucleation of $Ni(OH)_2$ on the graphene sheets.

To explain the formation of hierarchical flowerlike $Ni(OH)_2$ grown on graphene sheets, a possible formation mechanism based on experimental results is proposed, which is speculated to follow an adsorption-nucleation-coalescence-anisotropic growth-self-assembly mechanism (**Figure 4**). The main reactions in the system are as follows:[16]
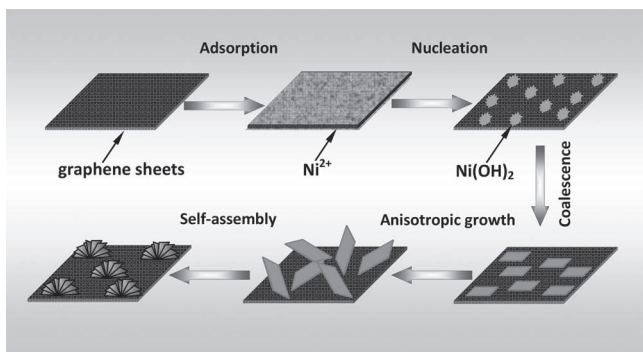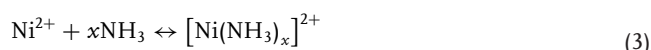
$$CO(NH_2)_2 + H_2O \leftrightarrow 2NH_3 + CO_2 \tag{2}$$

Makerials
Views
www.MaterialsViews.com

ADVANCED
FUNCTIONAL
MATERIALS
www.afm-journal.de

FULL PAPER

Figure 4. Schematic illustration for the possible formation of the flower-like $Ni(OH)_2$ nanostructures decorated on graphene sheets.

$$Ni^{2+} + xNH_3 \leftrightarrow \left[Ni(NH_3)_x\right]^{2+} \tag{3}$$

$$NH_3 + H_2O \leftrightarrow OH^- + NH_4^+ \tag{4}$$

$$Ni^{2+} + 2OH^- \leftrightarrow Ni(OH)_2 \tag{5}$$

Initially, the Ni^{2+} ions in the solution are adsorbed on the surface of graphene sheets because of the electrostatic attraction. Then, urea decomposes to NH_3 and CO_2 according to Equation 2. NH_3 can form a complex with Ni^{2+}, which decreases the concentration of free Ni^{2+} and accordingly reduces the growth rate of the crystals.[29,30] During the microwave heating process, urea can provide a steady OH^- ion supply through hydrolysis (Equation 2 and 4), which is favorable for the nucleation and the formation of ultrathin $Ni(OH)_2$ platelets based on the coalescence mechanism. From a thermodynamics perspective, the surface energy of an individual nanoplatelet is extraordinary high. In order to minimize the overall surface energy, the ultrathin platelets tend to self-assemble spontaneously to form 3D flowerlike $Ni(OH)_2$ architectures on the graphene sheets as the reaction continues further.[29]

Cyclic voltammetry (CV) is generally used to characterize the capacitive behavior of an electrode material. **Figure 5**a shows the typical CV curves of the as-prepared $Ni(OH)_2$/graphene composite at different scan rates in 6 M KOH aqueous solution. All the CV curves consist of a pair of strong redox peaks, indicating that the capacitance characteristics are mainly governed by Faradaic redox reactions, which is very distinct from that of electric double layer capacitors that usually produce a CV curve close to an ideal rectangular shape. The anodic peak (positive current density) occurred around 0.27 V (vs. Hg/HgO) indicates an oxidation process related to the oxidation of α-$Ni(OH)_2$ to γ-NiOOH, whereas the cathodic peak (negative current density) observed around 0.10 V (vs. Hg/HgO) corresponds to a reduction process following the Faradaic reactions of $Ni(OH)_2$:

$$\alpha\text{-}Ni(OH)_2 + OH^- \rightleftharpoons \gamma\text{-}NiOOH + H_2O + e^- \tag{6}$$

The symmetric characteristic of the anodic and cathodic peaks indicates the excellent reversibility of the $Ni(OH)_2$/graphene electrode. In addition, it can be seen that the shapes of these CV curves show almost no significant change as the

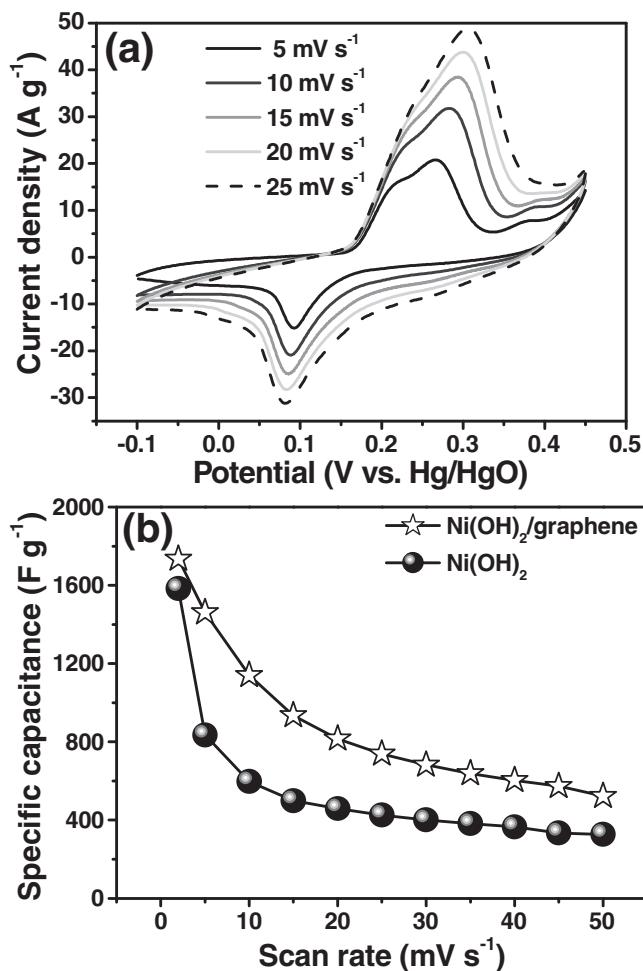**Figure 5.** a) CV curves of $Ni(OH)_2$/graphene composite at various scan rates in 6 M KOH. b) Specific capacitance of pure $Ni(OH)_2$ and $Ni(OH)_2$/graphene composite as a function of the scan rates based on the CV curves.

scan rates increase from 5 to 50 mV s^{-1}, implying the improved mass transportation, excellent electron conduction within the nanoparticles, and small equivalent series resistance. With increasing scan rates the potential of the oxidation peak shifts in the positive direction and that of the reduction peak shifts in the negative direction, which is mainly related to the internal resistance of the electrode.

The specific capacitance of the electrode can be calculated from the CV curves according to the following equation:

$$C = \left(\int I\,dV\right) / (vmV) \tag{7}$$

where C is the specific capacitance (F g^{-1}) based on the mass of the electroactive materials, I is the response current density (A cm^{-2}), V is the potential (V), v is the potential scan rate (mV s^{-1}), and m is the mass of the electroactive materials in the electrodes (g cm^{-2}). The specific capacitance of our as-prepared pure $Ni(OH)_2$ and $Ni(OH)_2$/graphene electrodes at different scan rates in 6 M KOH is presented in Figure 5b. It can

FULL PAPER

be seen that the specific capacitance of the Ni(OH)$_2$/graphene electrode is always higher than that of the pure Ni(OH)$_2$ electrode at different scan rates. A high specific capacitance of 1735 F g^{-1} can be obtained at 1 mV s^{-1} for the Ni(OH)$_2$/graphene electrode, which is comparable to those of previously reported values.[1,23,28,29] When the scan rate is increased to 50 mV s^{-1}, the specific capacitance of the Ni(OH)$_2$/graphene electrode is still 523 F g^{-1}, and retain 30% of its initial value with a scan-rate increase of 50 times, indicating the positive synergistic effect of graphene and Ni(OH)$_2$ in the composite. Moreover, the specific capacitance decreases gradually with increasing scan rate, which can be attributed to the diffusion effect limiting the diffusion and migration of the electrolyte ions within the electrode at high scan rates, resulting in low electrochemical utilization of the Ni(OH)$_2$ particles.[29] Therefore, the high capacitance of the Ni(OH)$_2$/graphene electrode can be ascribed to the synergistic effect of graphene and Ni(OH)$_2$. Firstly, the Ni(OH)$_2$ nanoplatelets on graphene sheets can effectively utilize their high pseudo-capacitance. Secondly, 3D interconnected nanoplatelets can form plenty of macropores, which is beneficial for the transport of electrolyte ions and charge transfer reactions. Finally, the graphene sheets in the composites can not only buffer the volume change of Ni(OH)$_2$ during the charging and discharging processes, but also preserve the high electrical conductivity of the overall electrode thanks to the excellent conductivity of graphene.[31] Because of the high performances of the Ni(OH)$_2$/graphene composite, it is highly desirable to develop a negative electrode material with superior electrochemical performance to assemble asymmetric supercapacitors with a wider voltage range and thus higher energy density than each of the components.

2.2. Negative Electrode Materials

Graphene has emerged as a promising material for applications in energy storage and conversion devices because of its high surface area and excellent electrical conductivity.[31,32] Recently, a KOH-activated graphene electrode has exhibited high specific capacitance (200 F g^{-1}) and rate performance in 1-butyl-3-methyl-imidazolium tetrafluoroborate/acetonitrile electrolyte, suggesting excellent electrochemical properties compared to chemically reduced graphene.[33] In our previous work, porous graphene was successfully synthesized using porous MgO sheets as the template using a chemical vapor deposition (CVD) approach.[34] TEM images of this porous graphene show that numerous wrinkled and folded regions and considerable mesopores (3-8 nm) with a Brunauer-Emmett-Teller surface area of 1654 m^2 g^{-1} are observed on the sheets (**Figure 6**a,b). Based on its unique structure, it is highly expected that porous graphene will exhibit an excellent electrochemical performance compared to chemically reduced graphene.

Compared to reduced graphene oxide, the CV curve of porous graphene measured in 6 M KOH solution still exhibits the typical rectangular shapes without obvious distortion even at a scan rate of 500 mV s^{-1} (**Figure 7**a), indicating an excellent capacitance behavior and fast diffusion of electrolyte ions into the electrode. Figure 7b shows the galvanostatic charge/discharge curves of the as-prepared sample. It can be clearly observed that all the curves are highly linear and symmetrical at various current
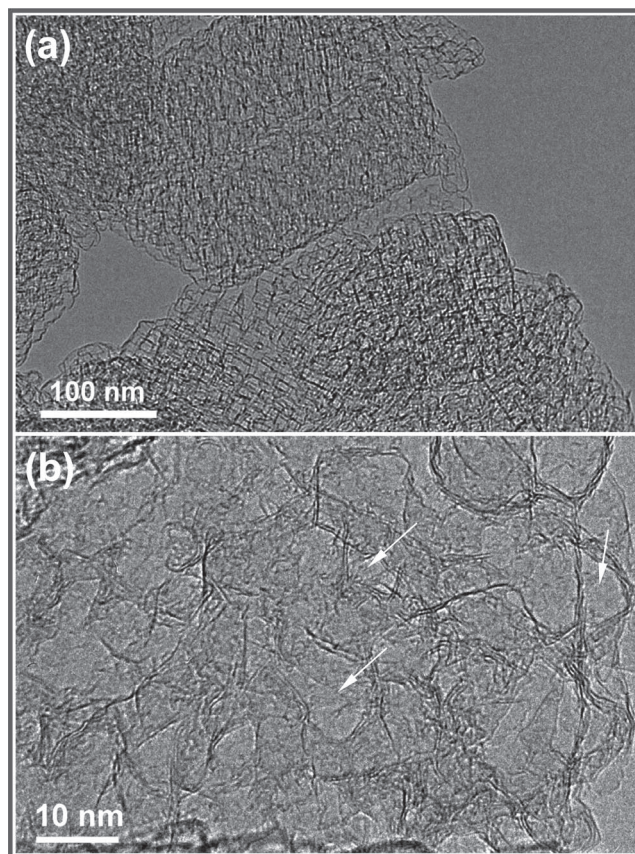

Figure 6. a) TEM and b) high-magnification TEM image of the porous graphene. The arrows indicate the existence of pores in the graphene sheets.

densities from 1 to 25 A g^{-1}, which is another typical characteristic of an ideal capacitor. No obvious iR drop is observed for any of the curves, meaning that the electrode has low internal resistance. The specific capacitance of porous graphene and chemically reduced graphene at different charge/discharge current densities is compared in Figure 7c. It can be seen that porous graphene not only exhibits high specific capacitance values but also maintains these high values much better at high current density compared to chemically reduced graphene. The porous graphene electrode shows a specific capacitance of 245, 236, 231, 220, and 209 F g^{-1} at different densities of 1, 2.5, 5, 10, and 25 A g^{-1}, respectively. Moreover, the porous graphene electrode exhibits an excellent long cycle life with only 5.9% capacitance loss after 2000 cycles (Figure 7d). These interesting results demonstrate that porous graphene delivers a high specific capacitance and superior rate performance compared to chemically reduced graphene because of its narrow mesopore distribution and open flat layer with high surface area.[34]

2.3. Asymmetric Supercapacitors

The high capacitance of the redox character of the Ni(OH)$_2$/graphene composite and the fast ion-transport property of the

www.MaterialsViews.com

ADVANCED
FUNCTIONAL
MATERIALS
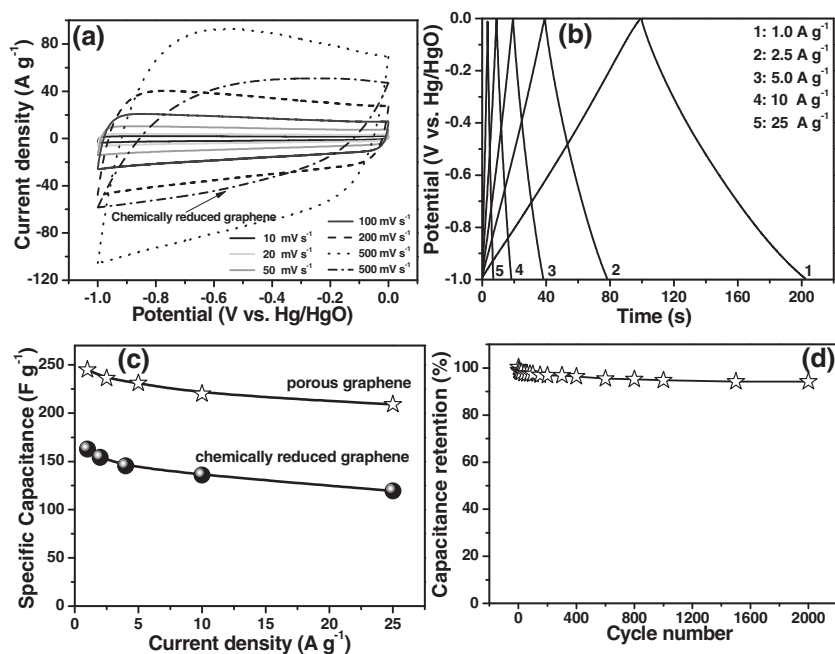www.afm-journal.de

FULL PAPER

Figure 7. a) CV curves of porous graphene at different scan rates in 6 M KOH. b) Galvanostatic charge/discharge curves of porous graphene at different constant current densities. c) Specific capacitance of porous graphene and chemically reduced graphene as a function of the current densities calculated from the corresponding discharge curve for each current density. d) Cycle performance of the porous graphene electrode at a scan rate of 200 mV s^{-1} in 6 M KOH aqueous solution.

graphene electrode. As a consequence, if the total cell voltage is expressed as the sum of the potential range for the Ni(OH)$_2$/graphene composite and that for the porous graphene material, the cell voltage could be extended up to 1.6 V in 6 M KOH aqueous solution for an asymmetric supercapacitor.[35–37] For supercapacitors, it is well-known that the charge balance between the two electrodes will follow the relationship $q_+ = q_-$, where the charge stored by each electrode usually depends on the specific capacitance (C), the potential range for the charge/discharge process (ΔE), and the mass of the electrode (m) following Equation 8:[38]

$$q = C \times \Delta E \times m \qquad (8)$$

and in order to obtain $q_+ = q_-$, the mass balancing will be expressed as follows:[38]

$$\frac{m_+}{m_-} = \frac{C_- \times \Delta E_-}{C_+ \times \Delta E_+} \qquad (9)$$

Based on the above analysis of the specific capacitance values and potential ranges found for the Ni(OH)$_2$/graphene composite and porous graphene, the optimal mass ratio between the two electrodes should be $m(\text{Ni(OH)}_2/\text{graphene})/m(\text{graphene}) = 0.44$ in the asymmetric supercapacitor cell.

Figure S3a (Supporting Information) exhibits the CV curves at different voltage windows for an asymmetric two-electrode cell assembled with the optimal mass ratio between the two electrodes in 6 M KOH aqueous electrolyte at a scan rate of 10 mV s^{-1}. It can be clearly seen that the fabricated asymmetric supercapacitor shows a good capacitive behavior with quasi-rectangular CV curves, even at voltages up to 1.6 V. When the operation voltage window is 1.0 V, the presence of the redox peaks indicate the pseudo-capacitive property of the supercapacitor because of the Faradaic reaction of Ni(OH)$_2$. Further increasing the operation voltage window to values as high as 1.6 V, more severe Faradaic reactions occur at the Ni(OH)$_2$/graphene electrode. Figure S3b (Supporting Information) depicts the specific capacitance of the fabricated asymmetric supercapacitor as a function of the operation voltage window. It was found that the specific capacitance greatly increases from 28.8 to 88.1 F g^{-1} as the operation voltage window range is increased from 1.0 to 1.6 V, which means that the stored energy and delivered power could be improved at least by 783% according to Equation 1. As a consequence, the overall performance of the supercapacitor could also be remarkably improved. As is generally known, operating at higher voltage will be favorable for reducing the number of devices in series required to reach the desired output voltage in practical applications.[10] Thus, we chose an operation voltage window of 1.6 V in 6 M KOH aqueous electrolyte to further investigate the superior electrochemical performance of the as-fabricated asymmetric supercapacitor in our subsequent research.

electric double-layer storage of the porous graphene led to the successful fabrication of an asymmetric capacitor using them as the positive and negative electrodes, respectively (Figure 1). To further evaluate the electrochemical properties and estimate the stable potential windows of the as-prepared Ni(OH)$_2$/graphene composite and porous graphene, we performed CV measurements on these two electrode materials in 6 M KOH using a three-electrode system at 20 mV s^{-1} before evaluating the asymmetric cell (Supporting Information Figure S2). The CV curve of the porous graphene electrode exhibited a relatively ideal rectangular shape and near mirror-image current response on voltage reversal, and no obvious redox peaks were observed, indicating a typical characteristic of a electric double-layer capacitor and excellent electrochemical reversibility. As for the CV curve for the Ni(OH)$_2$/graphene electrode, its shape is more complicated and very distinguished from that of the porous graphene, indicating that its capacitance mainly originates from the redox pseudo-capacitance of Ni(OH)$_2$. A pair of redox peaks could be clearly observed with the cathodic peaks at 0.10 V and anodic peaks around 0.27 V. The specific capacitance calculated from the CV curves using Equation 7 under these conditions is 816 F g^{-1} for the Ni(OH)$_2$/graphene composite, which is much higher than that of the porous graphene electrode (217 F g^{-1}). This significant difference can be explained by the fact that the overall capacitance of the Ni(OH)$_2$/graphene composite derives from the combined contribution of the primary redox pseudo-capacitance of Ni(OH)$_2$ and the electrical double-layer capacitance of graphene in the composite, whereas only the electrical double layer contributes toward the capacitance of the porous

**ADVANCED
FUNCTIONAL
MATERIALS**

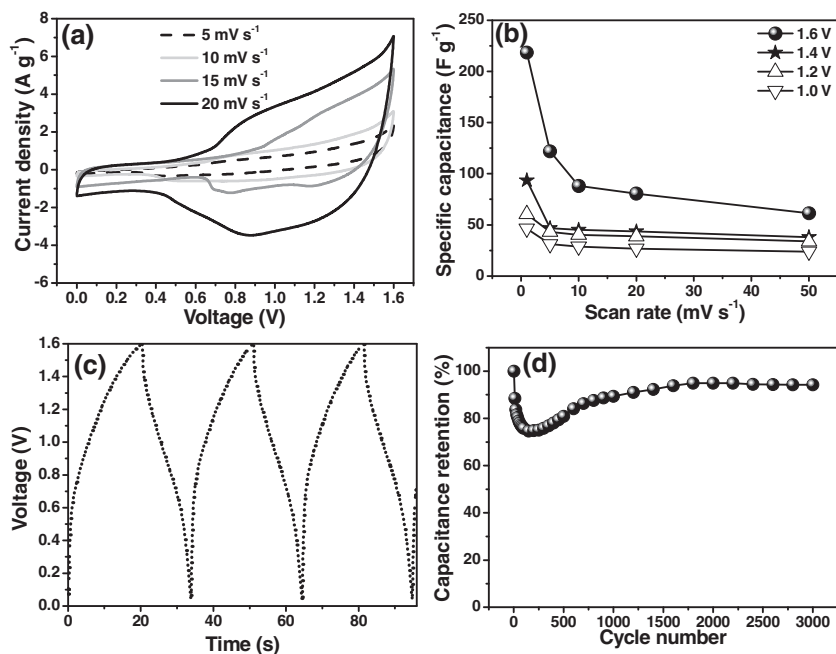www.afm-journal.de

Materials Views

www.MaterialsViews.com

Figure 8. a) CV curves of an optimized asymmetric supercapacitor in 6 M KOH electrolyte at different scan rates of 5, 10, 15, and 20 mV s⁻¹. b) Variation of specific capacitance at different scan rates for the asymmetric supercapacitor operated within different voltage windows. c) Galvanostatic charge/discharge curves of the asymmetric supercapacitor at a current density of 5 A g⁻¹. d) Cycle performance of the optimized Ni(OH)₂/graphene//porous graphene asymmetric supercapacitor within a voltage window of 1.6 V at a scan rate of 100 mV s⁻¹.

Figure 8a exhibits the CV curves of an optimized asymmetric supercapacitor at various scan rates of 5, 10, 15, and 20 mV s⁻¹ measured between 0 and 1.6 V in 6 M KOH aqueous electrolyte. The current-potential response is dependent on the potential as opposed to the potential-independent current response of an electrochemical capacitor based on a non-faradaic process. The specific capacitance of the asymmetric cell (based on the total mass of the active materials of the two electrodes) at different scan rates calculated from the CV curves using Equation 7 is presented in Figure 8b. The specific capacitance decreases gradually with increasing scan rate as diffusion limits the movement of electrolyte ions at high scan rates because of the time constraint and only the outer active surface can be utilized for charge storage, resulting in a lower electrochemical utilization of electroactive materials.[39] The higher specific capacitance could be obtained at higher operation voltage windows thanks to the redox reactions of Ni(OH)₂.[40] When the operation voltage window was 1.6 V, a maximum specific capacitance of 218.4 F g⁻¹ could be obtained at a scan rate of 1 mV s⁻¹, which is about 2.3, 3.6, and 4.7 times the specific capacitances obtained when operated at 1.4, 1.2, and 1.0 V, respectively. Importantly, it should be pointed out that the specific capacitance is calculated based on the total mass of the active material on both electrodes. The excellent performance of the Ni(OH)₂/graphene//porous graphene supercapacitor can thus be attributed to the high capacitance and rate performance as well as the synergistic effects of both the Ni(OH)₂/graphene composite and porous graphene electrodes.

Figure 8c shows the typical galvanostatic charging/discharging curves of our optimal asymmetric supercapacitor at a current density of 5 A g⁻¹ in 6 M KOH aqueous solution. A good linear relation of the charge/discharge potentials with time was found, indicating a rapid I–V response and small equivalent series resistance.[3] Additionally, from the typical isosceles triangular-shaped galvanostatic charge/discharge curve, it can be observed that the discharge curve is nearly symmetric with its corresponding charging counterpart, demonstrating the excellent electrochemical reversibility and good Coulombic efficiency.

As a long cycling life is an important requirement for supercapacitor applications,[41] a cycling-life test was carried out for the Ni(OH)₂/graphene//porous graphene asymmetric supercapacitor by repeating the CV test between 0 and 1.6 V at a scan rate of 100 mV s⁻¹ for 3000 cycles. Figure 6d shows the capacitance retention ratio of the asymmetric capacitor charged at 1.6 V as a function of the cycle number. It is worth noting that the specific capacitance sharply decreases after the initial 150 cycles (retained ca. 75.1% of its initial capacitance), which is probably related to pulverization and loss of electrical contact between the active material and the current as well as wettability issues.[42] The subsequent increase in capacitance can be related to an improvement in the surface wetting of the electrode by the electrolyte during extended cycling.[43] After 3000 cycles, the asymmetric supercapacitor displays an excellent long cycle life with only 5.7% deterioration of its initial specific capacitance, demonstrating superior long-term electrochemical stability. In addition, such cycling performance is highly competitive with those of some other asymmetric supercapacitors, such as Co(OH)₂//activated carbon (93% retention after 1000 cycles),[44] MnO₂//activated carbon in organic electrolyte (96% retention after 1000 cycles),[45] graphene/MnO₂//activated carbon nanofiber (97% retention after 1000 cycles),[3] LiNi₀.₅Mn₁.₅O₄//activated carbon (95% retention after 1000 cycles),[46] Ni(OH)₂//activated carbon (82% retention after 1000 cycles),[35] Ni(OH)₂/graphene//RuO₂/graphene (ca. 92% retention after 5000 cycles),[14] LiNi₁/₃Co₁/₃Mn₁/₃O₂//AC (ca. 80% retention after 1000 cycles),[47] graphene/MnO₂//graphene (79% retention after 1000 cycles),[9] Li₂MnO₄//activated carbon (ca. 95% retention after 20000 cycles),[48] and MnO₂//activated carbon in aqueous electrolyte (87.5% retention after 19500 cycles).[49]

The power density (P) and energy density (E) are generally used as important parameters to characterize the electrochemical performance of electrochemical cells.[3] The energy density at different average power density (Pₐᵥ) was calculated for our cells from the CV curves at different scan rates according to Equation 1 and 10:

$$P_{av} = \frac{E}{t} \tag{10}$$

Materials
Views
www.MaterialsViews.com

ADVANCED
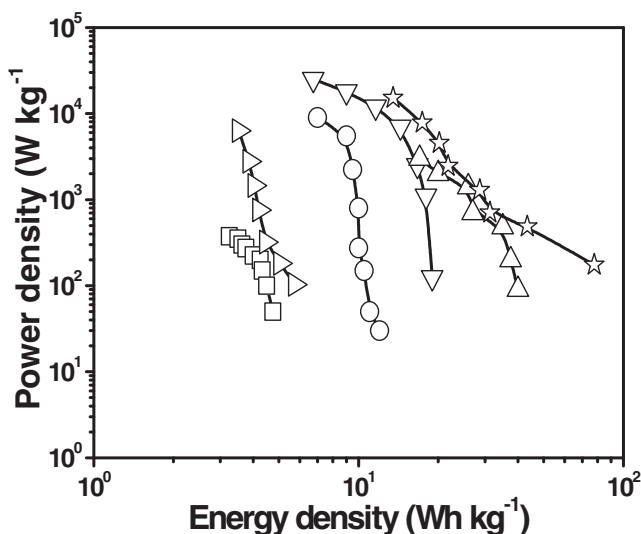FUNCTIONAL
MATERIALS
www.afm-journal.de

FULL PAPER

Figure 9. Ragone plot related to energy and power densities of the Ni(OH)$_2$/graphene//porous graphene asymmetric supercapacitor (☆) operated at 1.6 V in comparison to symmetric capacitors from commercial porous carbon (EC-600JD, □)[50] and porous graphene (▷), and several nickel-based asymmetric supercapacitors previously reported in the literature, namely NiO//carbon (○, ▽)[40,60] and Ni-Zn-Co oxide/hydroxide//carbon (△).[61]

where t is indicating the discharge time (s). **Figure 9** shows the Ragone plots of the as-fabricated asymmetric supercapacitors measured in the voltage window of 0–1.6 V at different scan rates. Although the specific energy density generally decreases with increasing specific power density, it is obvious that both the power density and energy density are significantly enhanced upon increasing the operation voltage from 1.0 to 1.6 V (Supporting Information Figure S4) as the energy density of a capacitor is governed by the specific capacitance and the maximum operational voltage.[5] It should be noted that the obtained maximum energy operated at 1.6 V is about 3, 6, and 12 times those of the cells operated at 1.4, 1.2, and 1.0 V, respectively. According to Equation 1, the considerably improved energy density can probably be ascribed to the high voltage and the increased capacitance because of Faradaic reactions. The Ni(OH)$_2$/graphene//porous graphene asymmetric supercapacitor with a cell voltage of 1.6 V can exhibit an energy of 77.8 Wh kg^{-1} at a power density of 174.7 W kg^{-1}, and still retains 13.5 Wh kg^{-1} at a power density of 15.2 kW kg^{-1}. In addition, this high energy density is much higher than that of symmetrical supercapacitors, such as activated carbon//activated carbon supercapacitors (<10 Wh kg^{-1}),[50–55] carbon nanotubes(CNTs)//CNTs supercapacitors (<10 Wh kg^{-1}),[56–59] graphene//graphene supercapacitors (ca. 9.1 Wh kg^{-1})[14] and porous graphene//porous graphene supercapacitors (ca. 5.7 Wh kg^{-1}) and some recently reported nickel-based asymmetric supercapacitors in aqueous electrolyte solutions, such as Ni(OH)$_2$/graphene//RuO$_2$/graphene (48 Wh kg^{-1}),[14] NiO//carbon (15-20 Wh kg^{-1}),[40,60] Ni-Zn-Co oxide/hydroxide//carbon (41.65 Wh kg^{-1}),[61] and Ni(OH)$_2$//activated carbon (42.3 Wh kg^{-1}).[35] Furthermore, it is worth noting that both the energy

and power performances of this asymmetric supercapacitor are highly competitive with Li-ion batteries and significantly superior to current electrochemical capacitors and Ni-MH batteries.

The superior electrochemical performance of the fabricated Ni(OH)$_2$/graphene//porous graphene asymmetric supercapacitor can be reasonably attributed to the synergistic effects between the positive and negative electrodes. The energy density of the asymmetric capacitor is significantly improved because of the high specific capacitance of the electrodes and the wide operation voltage window. On the other hand, the graphene materials in both electrodes demonstrate their distinctive features for asymmetric supercapacitors. Because of its excellent mechanical properties, good electrochemical stability, and superior conductivity, the graphene nanosheets can not only act as the support for the nanoscale flower-like Ni(OH)$_2$ grown on the sheets, but also maintain the mechanical integrity and high electrical conductivity of the overall electrode. On the other hand, using porous graphene with considerable mesopores (ca. 10 nm) as the negative electrode facilitates the transport of electrolyte ions and provides a larger surface area for charge-transfer reactions, ensuring high power density and excellent rate performance. Thus, pairing up Ni(OH)$_2$/graphene and porous graphene hybrid materials for asymmetrical supercapacitors represents a new approach to high-performance energy storage.

3. Conclusions

We have successfully developed an asymmetric supercapacitor using Ni(OH)$_2$/graphene and porous graphene as the positive and negative electrodes, respectively. The asymmetrical supercapacitor shows high specific capacitance, high energy density, and good cycling stability at an operating voltage of about 1.6 V in KOH aqueous electrolytes. It is shown that it is highly desirable to couple the Ni(OH)$_2$/graphene composite with porous graphene to produce supercapacitors with high energy and power densities. These encouraging findings can open up the possibility of graphene-based composites for numerous applications in asymmetric supercapacitors with high voltage, high energy, and high power densities to meet the diverse demands where high power and energy storage systems are required.

4. Experimental Section

Synthesis of Flowerlike Ni(OH)$_2$/Graphene Composite: Graphene sheets were prepared by chemical reduction of graphene oxide with hydrazine hydrate according to the literature.[25] The flowerlike Ni(OH)$_2$/graphene composite was synthesized using a microwave heating approach without any hard/soft templates or precipitate-controlling agents. In a typical synthesis, 0.1 g of graphene was added into 100 mL of distilled water and subjected to ultrasonic vibration to form a homogeneous suspension. Then 3.28 g of nickel (II) nitrate hexahydrate and 13.54 g of urea were added into the above graphene suspension and stirred for a while. Subsequently, the as-formed suspension was transferred into a microwave synthesis system (PreeKem, APEX) and subjected to microwave heating for 7 min under ambient atmosphere with a power of 700 W, and then cooled naturally to room temperature. Finally, the black deposit was filtered, washed several times with distilled water and alcohol, and dried at 100 °C for 12 h in a vacuum oven. For comparison,

ADVANCED
FUNCTIONAL
MATERIALS
www.afm-journal.de

www.MaterialsViews.com

FULL PAPER

pure Ni(OH)$_2$ was also synthesized by the same procedure as described above in the absence of graphene. The mass fraction of Ni(OH)$_2$ grown on graphene was 79 wt%, which was obtained by comparing the mass of the Ni(OH)$_2$/graphene composite with the mass of graphene used in the synthesis.

Synthesis of Porous Graphene: Porous graphene was prepared by a template CVD approach as described in our previous report.[34] Briefly, the quartz reactor was heated to 900 °C in an argon flow of 1000 mL min^{-1} at atmospheric pressure. When the reaction temperature was reached, CH$_4$ was introduced into the reactor at a flow rate of 800 mL min^{-1}. Then, the MgO template (ca. 30 g) was fed into the reactor over 5 min from the top hopper. After 10 min of carbon deposition, the CH$_4$ stream was turned off and the reactor was cooled to room temperature in an Ar atmosphere. The material obtained was purified by acid washing under reflux for 1 h to remove MgO. Finally, the resultant precipitate was filtered and dried overnight in an oven at 80 °C.

Characterization: The crystallographic structures of the materials were determined by a powder XRD system (TTR-III) equipped with Cu Kα radiation ($\lambda = 0.15406$ nm). XPS measurements were performed using a PHI 5700 ESCA spectrometer with a monochromated Al Kα radiation ($h\nu = 1486.6$ eV). All XPS spectra were corrected using the C 1s line at 284.6 eV. Curve fitting and background substraction were accomplished using Casa XPS version 2.3.13 software. The microstructure of the samples was investigated by TEM (JEOL JEM2010). Raman spectra were obtained on a Renishaw RM2000 Raman spectrometer with 457.9 nm wavelength incident laser light. FTIR spectroscopy was carried out on a Perkin Elmer Spectrum 100 spectrometer in a range of 600-4000 cm^{-1}.

Electrochemical Characterization: Electrodes used for the fabrication of asymmetric supercapacitors were prepared by mixing the electroactive material, carbon black, and poly(tetrafluoroethylene) with ethanol in a mass ratio of 75:20:5 to obtain a slurry. Then the slurry was pressed onto the nickel foam current collector (1 cm × 1 cm) and dried at 100 °C for 12 h. Each electrode contained about 3 mg cm^{-2} of electroactive material. To fabricate an asymmetric supercapacitor, the loading mass ratio of active material (Ni(OH)$_2$/graphene:porous graphene) was estimated to be 0.44 from the specific capacitance calculated from their CV curves. The electrochemical tests of the individual electrode were performed in a three-electrode cell, in which platinum foil and Hg/HgO electrodes were used as the counter and reference electrodes, respectively. The Ni(OH)$_2$/graphene cathode and porous graphene anode were pressed together and separated by a porous non-woven cloth separator. The electrochemical measurements of the asymmetric supercapacitor were carried out in a two-electrode cell at room temperature in 6 M KOH aqueous electrolyte solution (Figure 1). All of the above electrochemical measurements were carried out by a CHI 660C electrochemical workstation.

Supporting Information

Supporting Information is available from the Wiley Online Library or from the author.

Acknowledgements

Received: November 23, 2011
Published online: March 22, 2012

[1] H. Wang, H. S. Casalongue, Y. Liang, H. Dai, *J. Am. Chem. Soc.* **2010**, *132*, 7472.

[2] Z. Chen, Y. Qin, D. Weng, Q. Xiao, Y. Peng, X. Wang, H. Li, F. Wei, Y. Lu, *Adv. Funct. Mater.* **2009**, *19*, 3420.

[3] Z. Fan, J. Yan, T. Wei, L. Zhi, G. Ning, T. Li, F. Wei, *Adv. Funct. Mater.* **2011**, *21*, 2366.

[4] L. H. Bao, J. F. Zang, X. D. Li, *Nano Lett.* **2011**, *11*, 1215.

[5] Z. Chen, V. Augustyn, J. Wen, Y. W. Zhang, M. Q. Shen, B. Dunn, Y. F. Lu, *Adv. Mater.* **2011**, *23*, 791.

[6] B. E. Conway, *Electrochemical Supercapacitors: Scientific Fundamentals and Technological Applications*, Kluwer Academic/Plenum, New York **1999**.

[7] P. Simon, Y. Gogotsi, *Nat. Mater.* **2008**, *7*, 845.

[8] C. Liu, F. Li, L.-P. Ma, H.-M. Cheng, *Adv. Mater.* **2010**, *22*, E28.

[9] Z.-S. Wu, W. Ren, D.-W. Wang, F. Li, B. Liu, H.-M. Cheng, *ACS Nano* **2010**, *4*, 5835.

[10] A. Izadi-Najafabadi, S. Yasuda, K. Kobashi, T. Yamada, D. N. Futaba, H. Hatori, M. Yumura, S. Iijima, K. Hata, *Adv. Mater.* **2010**, *22*, E235.

[11] L. Demarconnay, E. Raymundo-Pinero, F. Beguin, *J. Power Sources* **2011**, *196*, 580.

[12] W. G. Pell, B. E. Conway, *J. Power Sources* **2004**, *136*, 334.

[13] P. C. Chen, G. Z. Shen, Y. Shi, H. T. Chen, C. W. Zhou, *ACS Nano* **2010**, *4*, 4403.

[14] H. Wang, Y. Liang, T. Mirfakhrai, Z. Chen, H. S. Casalongue, H. Dai, *Nano Res.* **2011**, *4*, 729.

[15] X. Y. Guan, J. C. Deng, *Mater. Lett.* **2007**, *61*, 621.

[16] L. P. Xu, Y. S. Ding, C. H. Chen, L. L. Zhao, C. Rimkus, R. Joesten, S. L. Suib, *Chem. Mater.* **2008**, *20*, 308.

[17] Y. Ren, L. Gao, *J. Am. Ceram. Soc.* **2010**, *93*, 3560.

[18] X. H. Liu, L. Yu, *Mater. Lett.* **2004**, *58*, 1327.

[19] X. H. Kong, X. B. Liu, Y. D. He, D. S. Zhang, X. F. Wang, Y. D. Li, *Mater. Chem. Phys.* **2007**, *106*, 375.

[20] F. S. Cai, G. Y. Zhang, J. Chen, X. L. Gou, H. K. Liu, S. X. Dou, *Angew. Chem. Int. Ed.* **2004**, *43*, 4212.

[21] K. Matsui, T. Kyotani, A. Tomita, *Adv. Mater.* **2002**, *14*, 1216.

[22] Q. Cheng, J. Tang, J. Ma, H. Zhang, N. Shinya, L.-C. Qin, *Carbon* **2011**, *49*, 2917.

[23] J. W. Lee, T. Ahn, D. Soundararajan, J. M. Ko, J.-D. Kim, *Chem. Commun.* **2011**, *47*, 6305.

[24] P. Jeevanandam, Y. Koltypin, A. Gedanken, *Nano Lett.* **2001**, *1*, 263.

[25] J. Yan, T. Wei, B. Shao, Z. J. Fan, W. Z. Qian, M. L. Zhang, F. Wei, *Carbon* **2010**, *48*, 487.

[26] M. C. Bernard, P. Bernard, M. Keddam, S. Senyarich, H. Takenouti, *Electrochim. Acta* **1996**, *41*, 91.

[27] C. Nethravathi, M. Rajamathi, *Carbon* **2008**, *46*, 1994.

[28] J. P. Liu, C. W. Cheng, W. W. Zhou, H. X. Li, H. J. Fan, *Chem. Commun.* **2011**, *47*, 3436.

[29] H. Jiang, T. Zhao, C. Z. Li, J. Ma, *J. Mater. Chem.* **2011**, *21*, 3818.

[30] C. Z. Yuan, X. G. Zhang, L. H. Su, B. Gao, L. F. Shen, *J. Mater. Chem.* **2009**, *19*, 5772.

[31] S. Park, R. S. Ruoff, *Nat. Nanotechnol.* **2009**, *4*, 217.

[32] Z. Fan, J. Yan, L. Zhi, Q. Zhang, T. Wei, J. Feng, M. Zhang, W. Qian, F. Wei, *Adv. Mater.* **2010**, *22*, 3723.

[33] Y. Zhu, S. Murali, M. D. Stoller, K. J. Ganesh, W. Cai, P. J. Ferreira, A. Pirkle, R. M. Wallace, K. A. Cychosz, M. Thommes, D. Su, E. A. Stach, R. S. Ruoff, *Science* **2011**, *332*, 1537.

[34] G. Ning, Z. Fan, G. Wang, J. Gao, W. Qian, F. Wei, *Chem. Commun.* **2011**, *47*, 5976.

[35] J. W. Lang, L. B. Kong, M. Liu, Y. C. Luo, L. Kang, *J. Solid State Electron.* **2010**, *14*, 1533.

[36] C. L. Qin, X. D. Bai, G. P. Yin, Y. X. Liu, Z. Jin, H. J. Niu, *Pigm. Resin Technol.* **2009**, *38*, 230.

[37] J. P. Zheng, *J. Electrochem. Soc.* **2003**, *150*, A484.

www.MaterialsViews.com

**ADVANCED
FUNCTIONAL
MATERIALS**

www.afm-journal.de

FULL PAPER

[38] V. Khomenko, E. Raymundo-Pinero, F. Beguin, *J. Power Sources* **2006**, *153*, 183.

[39] Z. J. Lao, K. Konstantinov, Y. Tournaire, S. H. Ng, G. X. Wang, H. K. Liu, *J. Power Sources* **2006**, *162*, 1451.

[40] D. W. Wang, F. Li, H. M. Cheng, *J. Power Sources* **2008**, *185*, 1563.

[41] Y. Hou, Y. W. Cheng, T. Hobson, J. Liu, *Nano Lett.* **2010**, *10*, 2727.

[42] G. X. Hu, C. X. Li, H. Gong, *J. Power Sources* **2010**, *195*, 6977.

[43] V. Ganesh, S. Pitchumani, V. Lakshminarayanan, *J. Power Sources* **2006**, *158*, 1523.

[44] L. B. Kong, M. Liu, J. W. Lang, Y. C. Luo, L. Kang, *J. Electrochem. Soc.* **2009**, *156*, A1000.

[45] H. Q. Wang, Z. S. Li, Y. G. Huang, Q. Y. Li, X. Y. Wang, *J. Mater. Chem.* **2010**, *20*, 3883.

[46] H. M. Wu, C. V. Rao, B. Rambabu, *Mater. Chem. Phys.* **2009**, *116*, 532.

[47] Y. Zhao, Y. Y. Wang, Q. Y. Lai, L. M. Chen, Y. J. Hao, X. Y. Ji, *Synth. Met.* **2009**, *159*, 331.

[48] Y. G. Wang, Y. Y. Xia, *J. Electrochem. Soc.* **2006**, *153*, A450.

[49] T. Brousse, P. L. Taberna, O. Crosnier, R. Dugas, P. Guillemet, Y. Scudeller, Y. Zhou, F. Favier, D. Belanger, P. Simon, *J. Power Sources* **2007**, *173*, 633.

[50] C. Zheng, L. Qi, M. Yoshio, H. Y. Wang, *J. Power Sources* **2010**, *195*, 4406.

[51] D. W. Wang, F. Li, M. Liu, G. Q. Lu, H. M. Cheng, *Angew. Chem. Int. Ed.* **2008**, *47*, 373.

[52] Q. T. Qu, L. Li, S. Tian, W. L. Guo, Y. P. Wu, R. Holze, *J. Power Sources* **2010**, *195*, 2789.

[53] V. Khomenko, E. Raymundo-Pinero, F. Beguin, *J. Power Sources* **2010**, *195*, 4234.

[54] Q. T. Qu, Y. Shi, S. Tian, Y. H. Chen, Y. P. Wu, R. Holze, *J. Power Sources* **2009**, *194*, 1222.

[55] Q. T. Qu, Y. Shi, L. L. Li, W. L. Guo, Y. P. Wu, H. P. Zhang, S. Y. Guan, R. Holze, *Electrochem. Commun.* **2009**, *11*, 1325.

[56] C. Yu, C. Masarapu, J. Rong, B. Wei, H. Jiang, *Adv. Mater.* **2009**, *21*, 4793.

[57] K. H. An, W. S. Kim, Y. S. Park, J. M. Moon, D. J. Bae, S. C. Lim, Y. S. Lee, Y. H. Lee, *Adv. Funct. Mater.* **2001**, *11*, 387.

[58] Y. Honda, T. Haramoto, M. Takeshige, H. Shiozaki, T. Kitamura, M. Ishikawa, *Electrochem. Solid-State Lett.* **2007**, *10*, A106.

[59] M. Kaempgen, C. K. Chan, J. Ma, Y. Cui, G. Gruner, *Nano Lett.* **2009**, *9*, 1872.

[60] H. Inoue, Y. Namba, E. Higuchi, *J. Power Sources* **2010**, *195*, 6239.

[61] H. L. Wang, Q. M. Gao, J. Hu, *J. Power Sources* **2010**, *195*, 3017.